ACCURACY ESTIMATION FOR LASER POINT CLOUD INCLUDING SCANNING GEOMETRY

P. Schaer [a, *], J. Skaloud [a], S. Landtwing [b], K. Legat [c]

[a] TOPO Lab, Ecole Polytechnique Fédérale (EPFL), Station 18, 1015 Lausanne, Switzerland
[b] Swissphoto AG, Dorfstrasse 53, 8105 Regensdorf-Watt, Switzerland
[c] Vermessung AVT – ZT-GmbH, Imst, Austria

ABSTRACT:

Individual points produced by airborne laser scanning (ALS) may have large variation in their accuracy, a fact that is often omitted in the subsequent derivation of digital terrain models. The accuracy of a single point is governed by three main factors: First, the errors due to the direct georeferencing of the laser beam; second, the measurement errors of the laser itself; third, the variation of the range-finder error due to the changing scanning geometry. The influence of the first two sources can be estimated by means of error propagation via known functional relations of georeferencing. Nevertheless, the influence of the third component is much harder to assess as it requires a-priori knowledge of the local terrain normal to compute the incident angle and the laser footprint. We propose a novel approach that analyzes the scanning geometry quantitatively by estimating the local terrain normal directly from the laser point cloud. Adding this information to the error propagation yields a final quality indicator that reflects not only the georeferencing quality but also the scanning geometry. The paper presents first results of the developed algorithm and assesses the possibilities to use such q-indicators within DTM/DSM-production. Their benefits are especially investigated for automated data classification and generation of DTM quality metadata.

1. INTRODUCTION

1.1 Motivation

Airborne laser scanning (ALS) is affected by many error sources, contaminating the laser point cloud with random and systematic errors. The analysis and the adequate modeling of these errors in the data processing is one of the major issues of research since ALS has become a widely used method for high quality DTM production.
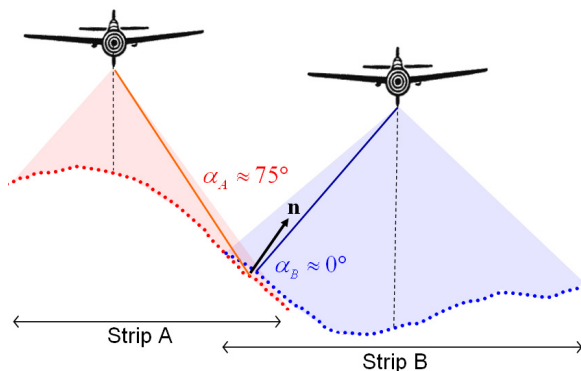

Figure 1: Adjacent strips with changing scanning geometry. The angle of incidence α of the laser beam is defined as the angle between the estimated surface normal vector **n** and the line of sight of the laser beam.

Conventional ALS error analysis considers the errors coming from the direct georeferencing of the laser beam (mainly due to navigation errors and system calibration) and the measurement errors of the laser itself (related to the range finder and the encoder angle measurements). These errors can be estimated by means of error propagation via the known functional relation between all observations and the calculated coordinates (Glennie, 2006; Landtwing, 2005). In such analyses, the accuracy of the range measurement is considered more or less constant.

Nevertheless, let us consider the situation presented in Figure 1. Intuitively, the individual points of this dataset, even if gathered with constant navigation and range measurement accuracy, must have a large variation in their accuracy. The points inside the strip overlap area are likely to have better quality when gathered within strip B (measurements that are almost perpendicular to the terrain) than within strip A, where the range measurements are affected by high incidence angles. This example highlights the problem related to poor intersection geometry and indicates that steep slopes can cause considerable difficulties to remote sensing, especially when measuring in a nadir-pointing configuration.

The impact of the incidence angle and the beam width on the total ALS error budget is not considered in standard error analysis. The presence of such errors is acknowledged (Airborne1, 2001; Alharthy et al., 2004; Huising and Pereira Gomes, 1998) but has not been modeled. The main reason for that are the difficulties in assessing the scanning geometry which in turn requires a-priori knowledge of the terrain slope and aspect. In this paper we propose a novel approach that analyzes the scanning geometry quantitatively by estimating the incident angle directly from the laser point cloud. This is achieved approximating the local terrain normal by means of eigenvalue decomposition of the covariance matrix obtained from neighboring points. This information provides the missing link to the subsequent computation of the 3D footprint as a function of the beam divergence and estimated incident angle.

* Corresponding author. Tel: +41 21 693 27 06 / Fax: +41 21 693 57 40 / email: philipp.schaer@epfl.ch

The influence of the footprint shape and size on the range accuracy is determined empirically and adds to the previously performed error propagation. Thus, every laser point receives a final quality indicator that reflects not only the quality of georeferencing but also the scanning geometry.

1.2 Paper outline

The organization of the paper is as follows: After giving definitions of ALS system errors, the functional model for their recovery is developed. The main part of the paper is devoted to the analysis of the scanning geometry. We present an efficient method to compute the incident angle, the resulting footprint and the influence on the point accuracy. We discuss the results of the algorithm on a sample dataset. The last part of the paper assesses the possibilities to use these accuracy estimates for DTM/DSM production. We especially investigate their benefits for automated data classification and generation of DTM quality metadata.

2. ERROR PROPAGATION

The calculation of ground coordinates for points from ALS observations is well documented in the literature (Baltsavias, 1999). Coordinates on the ground can be calculated by combining the information from the scanner, the integrated GPS/INS navigation system measurements and calibration parameters. The target coordinate equation for an arbitrary Cartesian mapping frame is given as:

$$\begin{bmatrix} x \\ y \\ z \end{bmatrix}^m = \begin{bmatrix} X \\ Y \\ Z \end{bmatrix}^m + \mathbf{R}_b^m \left[\mathbf{R}_s^b \rho \begin{pmatrix} \sin\theta \\ 0 \\ \cos\theta \end{pmatrix} + \begin{bmatrix} a_x \\ a_y \\ a_z \end{bmatrix}^b \right] \quad (1)$$

Where

$\mathbf{R}_b^m(r,p,y)$ is the attitude matrix from the IMU body frame to the mapping frame parameterized by roll, pitch and yaw

$\mathbf{R}_s^b(e_x,e_y,e_z)$ is the boresight matrix describing the angular offsets between the body frame and ALS frame

ρ, θ are the LiDAR range and the encoder angle

$[a_x\ a_y\ a_z]^T$ is the lever-arm offset between the IMU and ALS frame origins expressed in the body frame

There are numerous factors unique to every ALS system that affect the accuracy of the target coordinates. A detailed discussion of these different error sources can be found in (Morin, 2002) for example. For the purpose of our error analysis we will restrict the internal ALS error sources to random errors in distance and encoder angles only. We apply this reduction because most ALS manufacturers specify their expected accuracy in terms of these two main error components and do not specify the individual factors that contribute to the overall error. As a consequence, our error model involves 14 error states:

- 6 navigation errors: Namely we have the errors of the absolute positioning $(\sigma_X, \sigma_Y, \sigma_Z)$ and the orientation $(\sigma_r, \sigma_p, \sigma_y)$ of the sensor measured by GPS/INS. These errors can rapidly change in time due to changing GPS constellation and/or variable flight dynamics.
- 6 system calibration errors: Here we consider errors in the boresight angles $(\sigma_{ex}, \sigma_{ey}, \sigma_{ez})$ and in the lever arm

$(\sigma_{ax}, \sigma_{ay}, \sigma_{az})$. These components should change only with a change in system installation.
- 2 internal ALS errors: As mentioned above we only consider a range-finder error $(\sigma_\rho +$ ppm), having a constant and a scale-dependent part, and the error of the encoder angle (σ_θ). These errors are supposed to be intrinsic to every ALS system and are assumed to have a constant magnitude. The individual error sources and the involved frame systems for direct georeferencing of ALS measurements are displayed in Figure 2.
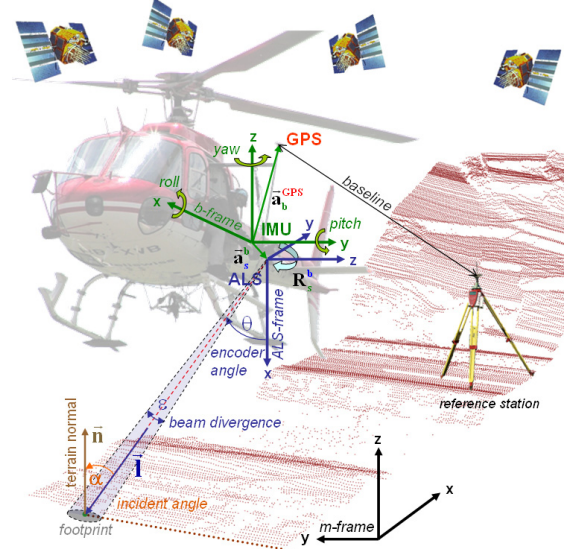

Figure 2: Used coordinate frames and error components for ALS point clouds

Propagating the random errors through the functional model of the laser georeferencing equation given by Eq. 1 yields a 3x3 point covariance matrix:

$$\mathbf{C}_{xyz} = \begin{bmatrix} \sigma_x^2 & \sigma_{xy} & \sigma_{xz} \\ \sigma_{xy} & \sigma_y^2 & \sigma_{yz} \\ \sigma_{xz} & \sigma_{yz} & \sigma_z^2 \end{bmatrix} = \mathbf{F} C_{ll} \mathbf{F}^T \quad (2)$$

We decompose the covariance matrix into horizontal and vertical components:

$$\sigma_{xy}^{nav} = \sqrt{\mathbf{C}_{xyz}(1,1) + \mathbf{C}_{xyz}(2,2)}, \ \sigma_z^{nav} = \sqrt{\mathbf{C}_{xyz}(3,3)} \quad (3)$$

Normally, the linear functional model (matrix $\mathbf{F}$) is obtained by linearising Eq. 1 by truncating a Taylor series expansion after the first term. In order to speed up the computations, we have constructed the functional model by algebraic derivation. Thereby, $\mathbf{F}$ takes the form of:

$$\mathbf{F}_{3\times14} = \left[\mathbf{F}_{pos} \middle| \mathbf{F}_{att} \middle| \mathbf{F}_{leverarm} \middle| \mathbf{F}_{bore} \middle| \mathbf{F}_{range} \middle| \mathbf{F}_{encoder} \right] \quad (4)$$

The stochastic model is given by

$$\mathbf{C}_{ll} = diag\left(\left[\sigma_X^2 \ \ \sigma_Y^2 \ \ \sigma_Z^2 \middle| \sigma_{roll}^2 \ \ \sigma_{pitch}^2 \ \ \sigma_{yaw}^2 \middle| \sigma_{a_x}^2 \ \ \sigma_{a_y}^2 \ \ \sigma_{a_z}^2 \middle| \sigma_{e_x}^2 \ \ \sigma_{e_y}^2 \ \ \sigma_{e_z}^2 \middle| \sigma_\rho^2 \middle| \sigma_\theta^2 \right] \right) \quad (5)$$

where the simplifying assumption was made that all individual error sources are uncorrelated.

3. ANALYZING THE SCANNING GEOMETRY

3.1 Modeling the relative power distribution

One of the intrinsic properties of a LiDAR scanner that strongly influences both the point cloud resolution and the positional uncertainty is the laser beam width. The apparent location of the range observation is along the centerline of the emitted beam. However, the actual point location cannot be predicted since it could lie anywhere within the projected beam footprint. A good demonstration of this uncertainty is presented in (Lichti and Gordon, 2004). Their estimate of uncertainty assumes a uniform level of laser power across the entire beam width diameter, which is typically not the case. Depending on the laser system, the waveform of a pulse may appear in different shapes.
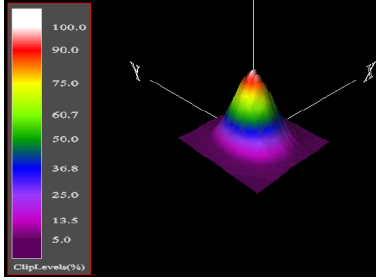

Figure 3: Relative power distribution of an optech ALTM LiDAR System (Glennie, 2006)

Figure 3 shows a typical power distribution of an outgoing laser pulse for the Optech ALTM LiDAR system. As can be seen, the power across the pulse is not uniform and can be approximately modeled as a symmetrical Gaussian distribution, where 100% of the energy is within the footprint. Approximating the footprint diameter to be $\pm 3\sigma$ (~99.7%), we can state that the 1-sigma level corresponds to one sixth of the footprint diameter. Based on this model we can now simulate the influence of the changing incidence angle on the spatial energy distribution (Fig. 4). The backscattered signal from the target surface will be a function of the integrated energy distribution across the whole footprint.
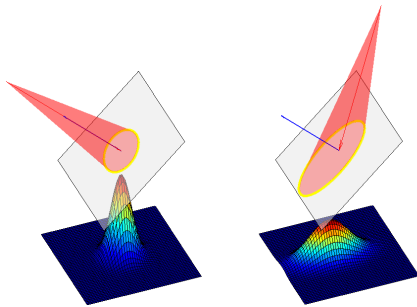

Figure 4: Influence of incident angle on relative power distribution: left: $\alpha = 0°$ - right: $\alpha = 60°$

3.2 Estimation of local terrain normal

To compute the incident angle and the footprint we need a-priori knowledge of the terrain normal. As shown in (Pauly et al., 2002) and (Bae and Lichti, 2004b) eigenvalue analysis of the covariance matrix of a local neighborhood can be used to estimate local surface properties. The covariance matrix $\mathbf{C}_{[3x3]}$ for a sample point is given by

$$\mathbf{C} = \begin{bmatrix} \mathbf{p}_{i_1} - \overline{\mathbf{p}} \\ ... \\ \mathbf{p}_{i_k} - \overline{\mathbf{p}} \end{bmatrix}^T \cdot \begin{bmatrix} \mathbf{p}_{i_1} - \overline{\mathbf{p}} \\ ... \\ \mathbf{p}_{i_k} - \overline{\mathbf{p}} \end{bmatrix}, i_j \in N_p \qquad (6)$$

Where

$\overline{\mathbf{p}}$ is the centroid of the neighborhood N_p including k-points (as shown in Fig. 5)

Let us consider the eigenvector problem:

$$\mathbf{C} \cdot \mathbf{v}_l = \lambda_l \cdot \mathbf{v}_l, l \in \{0,1,2\} \qquad (7)$$

Where $\mathbf{C}$ is symmetric and semi-definite. Therefore, its eigenvalues λ_l are real and the corresponding eigenvectors $\mathbf{v}_l$ form the orthogonal frame (Fig. 5) corresponding to the principal components (directions/orientations) of the point set defined by N_p. The eigenvalues present the variance in each direction. Accordingly, the eigenvector corresponding to the smallest variance (thus smallest eigenvalue) approximates the local terrain normal. This method is the first order approximation of the surface and a simple method to estimate surface normal vectors out of laser data.
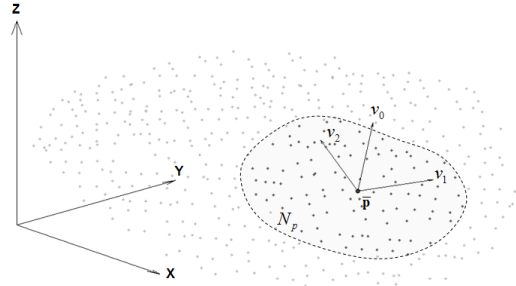

Figure 5: Neighborhood N_p of k-points and the computed principal directions

Knowing the terrain normal $\mathbf{n}$ and the laser direction $\mathbf{l}$ (Fig. 2), the incident angle α can be computed by

$$\alpha = \mathrm{acos}\left(\frac{\mathbf{l} \cdot \mathbf{n}}{|\mathbf{l}||\mathbf{n}|} \right) \qquad (8)$$

3.3 Computation of the 3D footprint

The footprint of a laser beam can be modeled as the ellipse formed by the intersection between a cone formed by origin $\mathbf{O}$, laser direction $\mathbf{l}$ and beam divergence ε and the local tangent plane with normal $\mathbf{n}$ (see Fig. 2 and Fig. 6). Once the main axes (major axis a and minor axis b) of the footprint are computed in 3D using cone canonicals, we can decompose the footprint into its maximal horizontal and vertical extension. Taking into account the assumption of symmetrical Gaussian power distribution within the footprint (see section 3.1), we can express the approximate positioning error (1σ) due to the scanning geometry by

$$\sigma_{xy}^{geom} = \frac{1}{3} \cdot \max\left\langle \left\| \begin{bmatrix} \mathbf{a}_x \\ \mathbf{a}_y \end{bmatrix} \right\|, \left\| \begin{bmatrix} \mathbf{b}_x \\ \mathbf{b}_y \end{bmatrix} \right\| \right\rangle \qquad (9)$$

and

$$\sigma_z^{geom} = \frac{1}{3} \cdot \max \left\langle \left| \left[\mathbf{a}_z \right] \right|, \left| \left[\mathbf{b}_z \right] \right| \right\rangle \qquad (10)$$
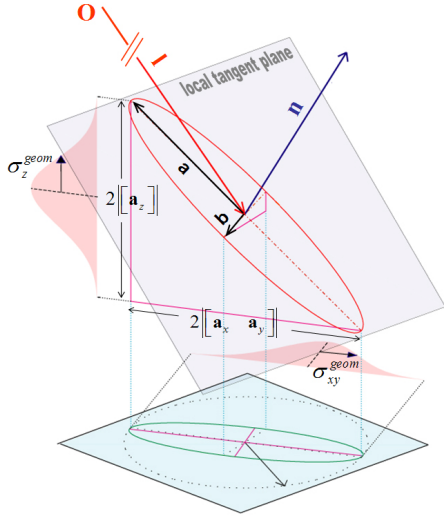

Figure 6: Decomposition of 3D footprint into its vertical and horizontal error components

4. GLOBAL Q-INDICATOR

Now that we have assessed all components contributing to the ALS error budget, we can regroup this information and construct one unique quality attribute for each laser measurement. This "q-indicator" q for a laser point i is constructed as accumulation of random errors coming from the error propagation of laser georeferencing equation (Eq. 2) and the scanning geometry analysis (Eqns. 9 and 10):

$$q_i = \sqrt{trace\left(\mathbf{C}_{xyz_i}\right) + \sigma_{xy_i}^{2\,geom} + \sigma_{z_i}^{2\,geom}} \qquad (11)$$

Obviously the correct scanning geometry depends entirely on the accurate estimation of the local terrain normal. Using the covariance method (Section 3.2), this estimation is only reliable when a point neighborhood approximately forms a plane surface. Laser points lying e.g. on vegetation have no clear geometric structure, hence the derived normal is geometrically not interpretable. As a consequence we need to filter out such points prior to the computation of the local terrain normal. In order to keep such evaluation completely autonomous, we apply a pre-classification of the data based on the local curvature criterion. As shown in (Bae and Lichti, 2004a), the geometric curvature M_{curv} of a point $\mathbf{p}_i$ can be estimated using the normal vectors of all points in the neighborhood $N_p(k)$:

$$M_{curv}(\mathbf{p}_i) = \frac{1}{k} \sum_{j=1}^{k} \left\| \mathbf{n}_{p_i} - \mathbf{n}_{neighbor\{j,pi\}} \right\| \qquad (12)$$

Where
k the size of the neighborhood
$\mathbf{n}_{pi}$ the normal of point pi
$\mathbf{n}_{neighbour\{j,pi\}}$ the normal of the j-th neighborhood-point of $\mathbf{p}_i$

In general, points on the ground or on buildings can be characterized by low curvature values (surface can often be approximated by a plane), whilst scanning points within vegetation and on roof edges generate high curvature values. These properties allow setting up a Boolean test to pre-classify laser points by applying a threshold *tol*:

$$low\_curvature\_point(\mathbf{p}_i) = \begin{cases} TRUE & if \ M_{curv}(\mathbf{p}_i) < tol \\ FALSE & if \ M_{curv}(\mathbf{p}_i) \geq tol \end{cases} \qquad (13)$$

The selection of the appropriate threshold depends mainly on the used neighborhood size k and the characteristics of the data set (point density, topography). Further information about the appropriate selection of such parameter can be found in (Bae et al., 2005).
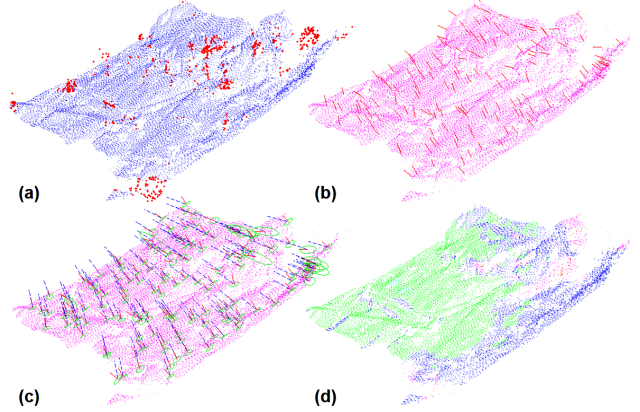

Figure 7: Steps for q-indicator computation: (a) pre-classification by threshold on local curvature; (b) computation of local normal; (c) computation incident angle and 3D footprint; (d) computation of final q-indicator

Now we dispose of all necessary elements to present the complete data workflow (summarized in Fig. 8). The error propagation is first carried out using the navigation data and their accuracy estimates (most standard GPS/INS software packages have options to output these estimates). After the point cloud generation in an arbitrary Cartesian mapping system, we build up a k-d tree for spatial indexing. This step considerably accelerates the querying (search of neighboring points to construct covariance matrix) of the data (Matton and Cools, 2004). After the computation of the local normal vector and curvature we proceed with the pre-filtering, removing all points above a certain curvature threshold. In the next step we analyze the scanning geometry, using the estimated local terrain normal, the laser direction and the beam divergence to compute the 3D footprint for the remaining laser points. In the last step we combine these data streams to one unique quality indicator (Eq. 11).
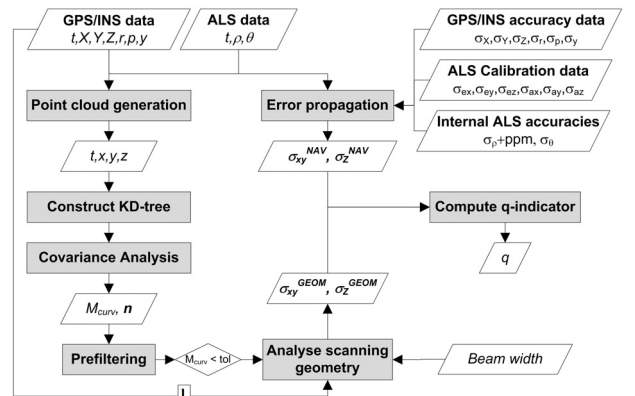

Figure 8: Generalized workflow for the computation of the q-indicator

5. TEST ON GURTNELLEN DATASET

The proposed approach was tested on a dataset flown in June 2006 near Gurtnellen (Canton Uri, Switzerland) using Optech's ALTM 3100 mounted in nadir configuration on a helicopter. The flight was carried out with the narrow beam setting (beam divergence = 0.3 mrad), a scan rate of 71 kHz and a mean flying height over ground of 1000 m. The dataset is characterized by very steep slopes (up to 90 deg), large elevation differences (up to 1000 m) within the same strip and unfavorable flight planning (flight direction parallel to slope contour). These characteristics are ideal to reveal quality variations due to changing scanning geometry.
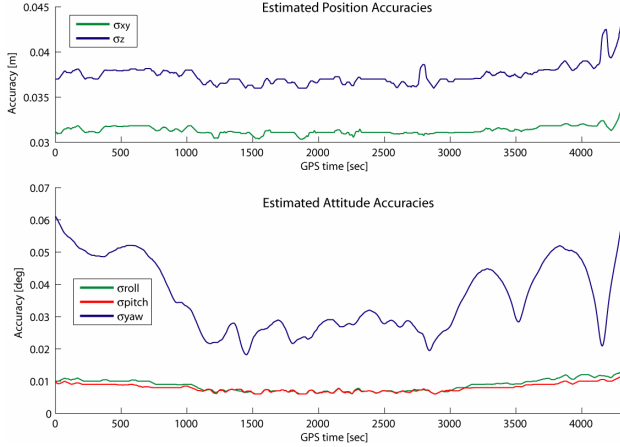

Figure 9: Estimated navigation (sbet) accuracies after GPS/INS integration for Gurtnellen dataset

The GPS/INS data was processed using PosProc software package from Applanix. Fig. 9 shows the results of the navigation accuracy estimates after smoothing. The system calibration was carried out by tachymetric measurements for the lever arm and using the LIBOR algorithm (Skaloud and Lichti, 2006) for the boresight. The intrinsic ALS error parameters were provided by the system manufacturer (Landtwing, 2005).

System Calibration parameters	
boresight	$\sigma_r = \sigma_p = 0.0002$ deg $\sigma_y = 0.003$ deg
leverarm	$\sigma_{ax} = \sigma_{ay} = \sigma_{az} = 0.01$ m
Intrinsic ALS parameters	
Range-finder	$\sigma_\rho = 0.09 + 0$ ppm
Encoder angle	$\sigma_\theta = 0.0018$ deg

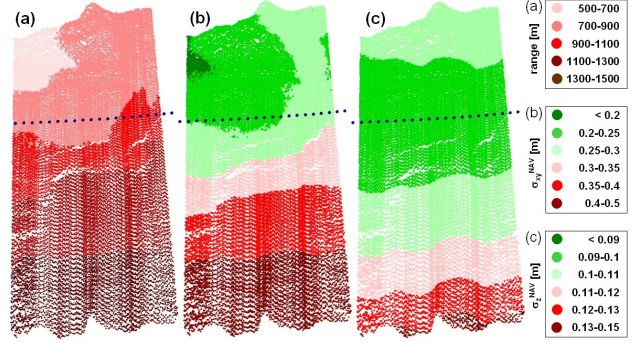Table 1: A priori ALS system accuracies

Figure 10: Estimated point accuracies by error propagation (without scanning geometry analysis) for extract of dataset: (a) ALS range length - (b) estimated horizontal accuracy (1σ) - (c) estimated vertical accuracy (1σ). The blue dots represent the projected helicopter positions.

Figure 10 illustrates the distribution of errors modeled by error propagation (Section 2). The flight presents a similar set-up as depicted for strip A in Fig. 1. The range **(a)** in nadir is about 1000 m, while in the extremities of the swath it oscillates from about 500 m (upper part) to 1500 m (lower part) respectively. We observe that the horizontal accuracy **(b)** is mainly governed by the absolute value of the range. The vertical accuracy **(c)** however, is also strongly influenced by the encoder angle. The best vertical accuracy is achieved in the nadir. Generally, the point accuracy due to the navigation error decreases with increasing range and encoder angle. It is also worth mentioning that the accuracy variations follow a very homogenous pattern with no sudden changes.
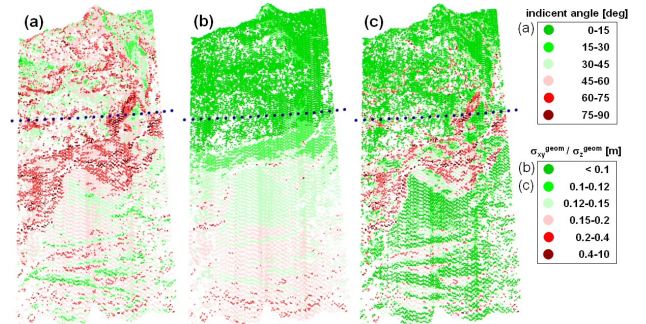

Figure 11: Impact of scanning geometry on the target accuracy: (a) computed laser incident angles (in degrees) - (b) horizontal geometric accuracy (1σ) - (c) vertical geometric accuracy (1σ). The vegetation points have been previously removed.

The upper figure demonstrates the results of the scanning geometry analysis (as described in Section 3.3). Unlike the navigation accuracy estimates (Fig. 10), the data in Fig. 11 has a very inhomogeneous character. The results of the scanning geometry depend directly on the terrain topography; therefore very abrupt changes in the scanning quality can occur. The dataset presents a large variation in the incident angles **(a)**, especially in the middle part (rock faces with slopes up to 70°, causing high incidence angles). Correspondingly we expect strong accuracy degradation in this region mainly in the vertical component. The plot of the vertical accuracy **(c)** affirms this assumption. The horizontal accuracy **(b)** has a slightly different behavior. Here, the absolute range value is the predominant factor, as the horizontal footprint size is proportional to the

distance of the laser head to the ground point. Therefore, the quality degradation is higher towards the lower part of the slope (similarly to Fig. 10-b).
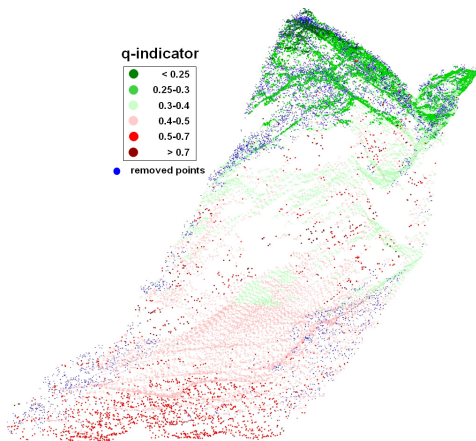

Figure 12: Isometric view on the Gurtnellen data, color coded by the q-indicator (green = best, red = worst)

Fig. 12 shows the results of the final q-indicator computation in an isometric view. No q-value was computed for the points in blue (vegetation points, sorted out by pre-filtering). Although the navigation accuracy was almost constant, large discrepancies in the point cloud accuracy occur, mainly due to variable range length and scanning geometry. Generally speaking, the quality of the data is approximately three times worse in the lower part of the strip than in its upper part. Nevertheless, the worst degradations can be found in the very steep middle part.

6. USE OF Q-INDICATORS IN DSM/DTM-PRODUCTION

The existence of such quality indication for each laser point offers variety of options for increasing efficiency and quality in the standard ALS DSM/DTM production process. We highlight some of them in the following paragraphs.

6.1 Strip Adjustment

The analysis of inter-strip discrepancies in the overlap areas and subsequent derivation of "field calibration" values can be considered as a standard procedure in state-of-the-art DSM/DTM production workflows. It estimates orientation and scale correction for the whole data set (e.g. to correct for residual boresight errors) or position shifts for individual flight lines (e.g. to compensate biases in the GPS solution).

However, most algorithms used in practice (Burman, 2002) consider all points – at least within the same strip – as having the same quality. As previously shown, this assumption is not correct. Especially the points laying on the edges of the flight lines – exactly where overlap analysis usually occurs – are of degraded accuracy, most notably in inclined terrain.

Ignoring this fact makes it more difficult to quickly reach a converging solution and can even lead to wrong results. This can be the case when clusters of simply less accurate points (due to scanning geometry) influence the solution in a way that degrades the adjustment parameters. Applying incorrect adjustment values to the whole data set can end up in corrupting parts of previously good data.

The use of the q-indicator to weight points when solving for strip adjustment parameters can lead to improved accuracy and reliability of the results, thus enhancing the quality of the derived product.

6.2 Automated Ground Classification

Most of today's ground classification algorithms (Sithole and Vosselman, 2003; Soininen, 2005) show a high affinity towards low points, regardless of their origin and quality.

Using the q-indicator – and possibly the pre-classification according to local curvature – could increase the robustness of automated ground classification by considering only "good quality" points for the first iteration and adding points of lower quality subsequently.

Such an approach obviously does not have a significant effect in areas with only low-quality data but can help minimize problems with ground classification in strip overlap areas, especially when adjacent strips match badly due to different quality.

6.3 Manual Editing

To reach a DTM/DSM of high quality, sometimes manual editing is still necessary, particularly for data representing complex topography. Here, critical areas are examined visually and improved by reclassifying groups of points based on subjective decisions.

Introducing q-indicators as an additional basis for deciding which points to prefer in manual classification (e.g. ground/non-ground) can help the operator to make more objective decisions, which in term improves the quality of the end product.

6.4 Metadata Generation

With ALS becoming a well-established technology, the users start demanding good documentation about the data origin, quality and processing history. (Luethy, 2007) shows that nowadays the compilation of metadata must be considered as an integral part of the ALS production workflow.

Being able to document the expected quality quickly and automatically by explicitly demonstrating the compliance (or lack of it) with the project specifications, certainly qualifies as a valuable asset when delivering comprehensive metadata to the client.
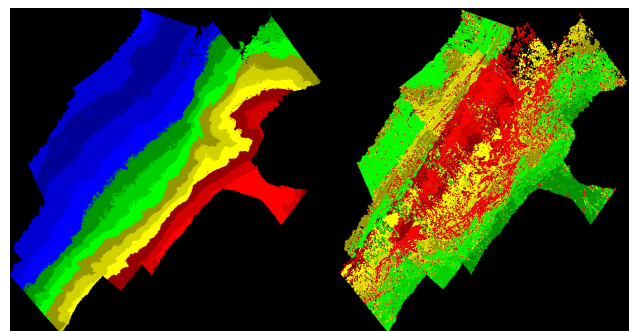

Figure 13: Whole Gurtnellen data set color coded by elevation (left) and the q-indicator (right: green = best, red = worst)

Fig. 13 illustrates an example of generating metadata by color coding the point cloud by the value of the q-indicator. The right plot in this figure offers obtaining an impression about the accuracy distribution over the data set rapidly when highlighting areas with quality problems. In this data set the

main quality problems (dark red in the middle part) are due to large incident angles on extremely steep terrain.

7. CONCLUSIONS AND OUTLOOK

We have presented an algorithm capable of analyzing the accuracy of ALS data and providing a realistic estimate of the magnitude of error on the ground. The analysis of the scanning geometry allows the detection of unfavorable scan patterns and assesses their effects on data quality. We have introduced the concept of a unique quality attribute (q-indicator) for every single laser measurement and shown its value in practice. However, at the moment we consider this q-indicator as purely qualitative. The obtained results are to be controlled independently, which will be subject to further research. Nevertheless, we have shown that such q-indicator can be a very valuable tool within ALS data production. Data classification, strip adjustment and generation of LIDAR quality metadata can all profit from considering such a parameter.

There remain some open questions within the ALS error modeling that need to be addressed. At the moment the presented stochastic model does not consider correlation between the parameters, although it is known that the GPS coordinates and the IMU attitude angles are highly correlated among each other and in time. Another potential problem is the dependency of range accuracy on the reflectivity of the target and the amount of backscattered energy. Empirical tests have shown that the range finder accuracy is highly decreased on surfaces with low reflectivity (thus low intensity). As most ALS systems measure and store the intensity values, it would be theoretically possible to incorporate the target reflectivity into the general error model.

8. ACKNOWLEDGMENT

REFERENCES

Airborne1, 2001. LiDAR ACCURACY; AN AIRBORNE 1 PERSPECTIVE, Airborne 1 Corporation, El Segundo, California, USA.

Alharthy, A., Bethel, J. and Mikhail, E.M., 2004. Analysis and Accuracy Assessment of Airborne Laserscanning System, XXth ISPRS Congress, Istanbul, Turkey, pp. 144-149.

Bae, K.-H., Belton, D. and Lichti, D., 2005. A framework for position uncertainty of unorganised three-dimensional point clouds from near-monostatic laser scanners using covariance analysis, Proceedings of the ISPRS Workshop "Laser scanning 2005", Enschede, the Netherlands.

Bae, K.-H. and Lichti, D., 2004a. Automated Registration of Unorganised Point Clouds from Terrestrial Laser Scanners. In: O. Altan (Editor), XXth ISPRS Congress, Istanbul.

Bae, K.-H. and Lichti, D., 2004b. Edge and Tree Detection from Three-dimensional Unorganised Point Clouds from Terrestrial Laser Scanners, 12th Australian Remote Sensing and Photogrammetry Conference, Fremantle, Australia.

Baltsavias, E.P., 1999. Airborne laser scanning: basic relations and formulas. ISPRS Journal of Photogrammetry and Remote Sensing, 54(2-3): 199-214.

Burman, H., 2002. Laser strip adjustment for data calibration and verification. International Archives of Photogrammetry and Remote Sensing, 34(3A): 67-72.

Glennie, C.L., 2006. Rigourous 3D Error Analysis of Kinematic Scanning LIDAR Systems. Terrapoint USA Inc., The Woodlands.

Huising, E.J. and Pereira Gomes, L.M., 1998. Errors and accuracy estimates of laser data acquired by various laser scanning systems for topographic applications. ISPRS Journal of Photogrammetry and Remote Sensing, 53(5): 245-261.

Landtwing, S., 2005. Airborne Laser Scanning: Genauigkeitsinformationen für den Auswertungsprozess, Swiss Federal Institute of Technology (ETH), Zürich, 83 pp.

Lichti, D. and Gordon, S.J., 2004. Error Propagation in Directly Georeferenced Terrestrial Laser Scanner Point Clouds for Cultural Heritage Recording. In: FIG (Editor), FIG Working Week, Athens, Greece.

Luethy, J., 2007. Entwicklung eines Qualitätsmodells für die Generierung von Digitalen Geländemodellen aus Airborne Laser Scanning, Swiss Federal Institute of Technology, Zürich, Switzerland.

Matton, M. and Cools, R., 2004. A comparison of different k-nearest neighbour algorithms with performance results on speech data, Department of Computer Science, Katholieke Universiteit, Leuven, Belgium.

Morin, K., 2002. Calibration of Airborne Laser Scanners, University of Calgary, Calgary, Canada, 134 pp.

Pauly, M., Gross, M. and Kobbelt, L.P., 2002. Efficient simplification of point-sampled surfaces, IEEE Conference on Visualization, Boston.

Sithole, G. and Vosselman, G., 2003. Comparison of Filtering Algorithms, ISPRS working group III/3 workshop '3-D reconstruction from airborne laser scanner and InSAR data', Dresden, Germany.

Skaloud, J. and Lichti, D., 2006. Rigorous approach to bore-sight self calibration in airborne laser scanning. ISPRS Journal of Photogrammetry and Remote Sensing, 61(1): 47-59.

Soininen, A., 2005. Ground Classification. Presentation available on the web site of TerraSolid Inc., Finland.